

Analysis of energetic particle transport: diffusion and phase-space barriers

N. Carlevaro,¹ M.V. Falessi,^{1,2} G. Montani,^{1,3} and Ph. Lauber⁴

¹*ENEA, Nuclear Department, C. R. Frascati, Via E. Fermi 45, Frascati, 00044 Roma, Italy*

²*Istituto Nazionale di Fisica Nucleare (INFN), Sezione di Roma, P.le Aldo Moro 2, 00185 Roma, Italy*

³*Physics Department, "Sapienza" University of Rome, P.le Aldo Moro 5, 00185 Roma, Italy*

⁴*Max Planck Institute for Plasma Physics, Boltzmannstrasse 2, D-85748 Garching, Germany*

A reduced 1D model describing the non-linear hybrid LIGKA/HAGIS simulations was developed and successfully tested in [1] addressing the ITER 15MA baseline scenario. In this paper, we introduce a detailed phase-space and statistical analysis to characterize the emerging transport regimes. Deviations from purely normal diffusive dynamics is quantitatively analyzed, indicating the limitations of the usual quasi-linear description of energetic particle turbulent transport. Beside the emergence of a very complex dynamics of overlapping resonances and substructure formation, this analysis reinforces the evidence of avalanche excitation and energy transfer between modes.

I. INTRODUCTION

Instabilities excited by energetic particles (EPs) constitute one of the primary challenges in magnetic confinement fusion. Specifically, EPs can facilitate cross-scale interactions resulting in inherently multi-scale phenomenologies [2–7]. Numerical methods, such as global hybrid-kinetic or fully gyro-kinetic simulations, are extremely resource-intensive and time-consuming when applied to both current and next generation devices [8, 9]. Consequently, reduced models for relaxation are of crucial importance. Examples of these models include the kick model [10], the critical gradient scheme [11], the QL theory and its extensions [12, 13] and the recent ATEP model [14–16]. One of the key challenges of these models is accurately identifying and incorporating transitions between different regimes, due to the intermittent nature of EPs transport [17].

When dealing with multiple discrete Alfvén eigenmodes (AEs) with strongly overlapping resonances, the commonly used approach is based on quasi-linear (QL) models [18, 19] (see also [11, 13, 20, 20–23]). However, while QL theory can predict EP redistribution in certain scenarios [3], making accurate predictions for stochastization thresholds and transport in the ITER context requires detailed understandings of the underlying physics and the phase space characteristics of the EP distribution [10, 24–26]. In particular, transport processes in burning plasmas can exhibit high levels of non-locality and anisotropy in the phase space and, due to this complexity, simple diffusion equations become questionable [12, 27]. Additionally, the linearly stable part of the fluctuating spectrum is found to significantly influence EP dynamics [3, 28, 29] (see also [30, 31]).

The 1D bump-on-tail (BoT) paradigm has often been used to mimic the non-linear interplay between EPs and Alfvénic fluctuations [4, 32–35] (see also [36–38], for application of the Hamiltonian formulation of the BoT in other context of plasma physics). In [28], an analysis of the ITER 15MA baseline scenario suggests that realistic non-linear simulations are not accurately characterized by QL predictions, as they fail to reproduce typical avalanche phenomena [18, 39, 40]. Instead, this was captured by the 1D reduced description introduced in [1]. A mapping procedure linking the radial coordinate of the realistic 3D scenario to the velocity dimension of the BoT paradigm, described by a Hamiltonian beam-plasma model [3, 29, 41], has been defined and successfully tested against EP profile relaxation predictions from LIGKA/HAGIS simulations [42, 43].

In this paper, we provide a detailed characterization of the transport associated to the cascade process mentioned above, observed for the ITER 15MA baseline in the presence of the least damped 27 toroidal AEs (TAEs). In order to analyze the transport phenomenology in the phase space, we implement the Lagrangian Coherent Structure (LCS) technique [44]. LCSs divide the particle phase-space into macro-regions where fast mixing transport processes occur and, for this reason, they are routinely used to describe transport processes in a wide range of contexts and, specifically, to plasma physics in [41, 45–53]. The use of this methodology provides an immediate representation of the mechanism behind the cascade process. In particular, the formation of a stiff gradient at the boundary of the plateau region drives the development of elongated LCS and, consistently, enhances transport while exciting at the same time the sub-dominant part of the spectrum through non-linear wave-particle interactions. This scenario differs significantly from a constructed benchmark case, in which the the spectrum is globally unstable.

The relaxation of the distribution function is then analyzed by tracking the mean square displacement (MSD) of test particles over time. We show how particles related to the cascade phenomenon exhibit super-diffusive transport. This indicates that, when stable modes are destabilized, a complex transport pattern is generated that may require a fully-nonlinear treatment of EPs. This analysis confirms and deepens the results of previous studies, challenging the applicability of QL theory for sub-dominant spectrum generated transport. An additional evidence of the non-diffusivity of transport is provided by the analysis of phase-space fluxes. Summarizing, the present study describes

some of the fundamental factors governing distinct EPs transport regimes in fusion plasmas. The ability to identify indicators linked to cascade phenomena is essential for predicting these events in experiments and reduce the need for costly nonlinear simulations.

The paper is organized as follows. In Sec. II, the 1D reduced model is introduced and applied to the EP dynamics of the ITER 15MA baseline scenario. A benchmark case is also discussed. In Sec. III, the LCS technique is applied to characterize the dynamics in the phase space and the transport barriers of both systems. In Sec. IV, a statistical analysis of tracer dynamics and the study of the fluxes are addresses to define the nature of the underlying transport processes.

II. 1D REDUCED MODEL FOR AE DRIVEN TURBULENCE

In [1], the BoT model is used as a reduced scheme for quantitatively describing the dynamics of EP interacting with AEs. In this section, we outline the basic ingredients and the relevant outcomes of the reduced model when applied to the 15MA ITER baseline scenario addressed in [28].

The radial EP redistribution due to AEs is modeled implementing a linear one-to-one map between the radial coordinate s and the velocity u of the BoT system. The latter addresses a fast charged particle beam interacting with a 1D plasma considered as a cold dielectric medium, which supports longitudinal electrostatic waves. Here and in the following, all quantities are dimensionless and, in particular, s denotes the square root of the normalised poloidal flux. The linear correspondence is derived locally for a single resonance [1] and it reads $u = (1 - s)/\ell^*$, where ℓ^* is an arbitrary constant defining the spectral features as described below. We assume this relation to be valid in the whole radial domain and we remark that the reduced phase space describing wave-particle trapping phenomena is defined by $(x, u) \rightarrow (x, s)$, where x represents the spatial dimension of the BoT model. The reduced representation of the AEs corresponds to the modes $\phi_j(\tau)$, having frequency ω_j , linear drive γ_{Dj} , damping rate γ_{dj} and mode number ℓ_j (here, τ represents the normalized time in plasma frequency units). Mode numbers are integers set by the following resonance conditions: $\ell_j = \ell^*/(1 - s_{rj})$, where s_{rj} denotes the AE resonant radii and ℓ^* can be arbitrarily fixed in order to have enough distinct integers ℓ_j to properly represent the AE spectral density.

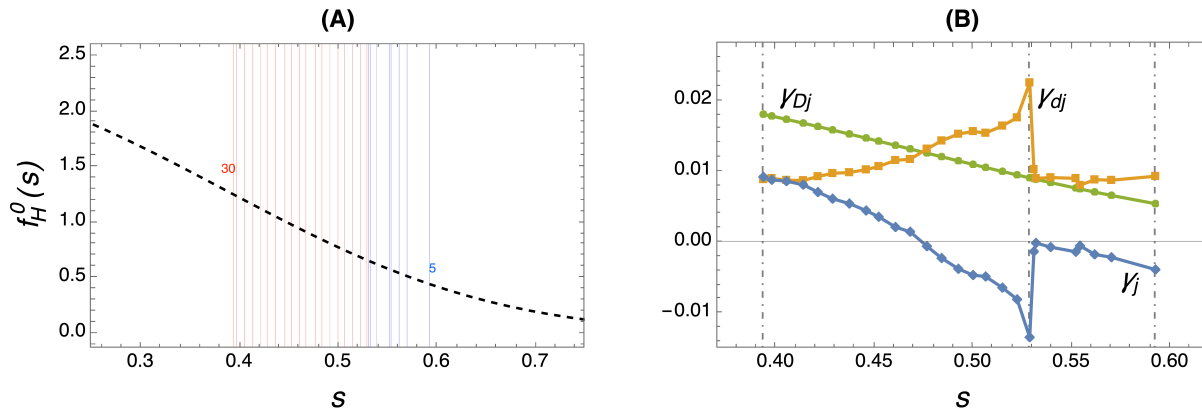


FIG. 1: Panel A — Initial EP profile f_H^0 (dashed black) in arbitrary units as a function of s from Eq.(1). Colored vertical lines indicate resonance positions: high- n_{AE} branch (HnB) in red, low- n_{AE} branch (LnB) in blue (for the sake of clarity, we also indicate the position of $n_{AE} = 30$ and $n_{AE} = 5$, the extremes of the spectrum). Panel B — Growth rates γ_j , linear drives γ_{Dj} and damping γ_{dj} (scaled data from [28]), as a function of the resonance position of the corresponding mode. γ_{Dj} are evaluated from Eq.(2) with $\eta = 0.007$. Gray dashed vertical lines indicate the HnB and LnB resonant regions.

The typical initial EP distribution is represented by a slowing down profile [28]

$$f_H^0(s) = f_H(0, s) = B_1 \operatorname{Erfc}[B_2 + sB_3], \quad (1)$$

where B_1, B_2, B_3 are constants, and the linear stability/instability of the mode $\phi_j(\tau)$ is governed by the following relation:

$$2(\omega_j + i\gamma_{Dj} - 1) + \frac{\eta\ell^*}{R\ell_j} \int_{-\infty}^{+\infty} ds \frac{\partial_s f_H^0(s)}{\ell_j(1-s)/\ell^* - \omega_j - i\gamma_{Dj}} = 0, \quad (2)$$

where η is a free parameter of the model (here $R = \int ds f_H^0$). Such a quantity can be set by analyzing the effective wave-particle power exchange of the most resonant particles. In fact, due to the reduced dimensionality of the model

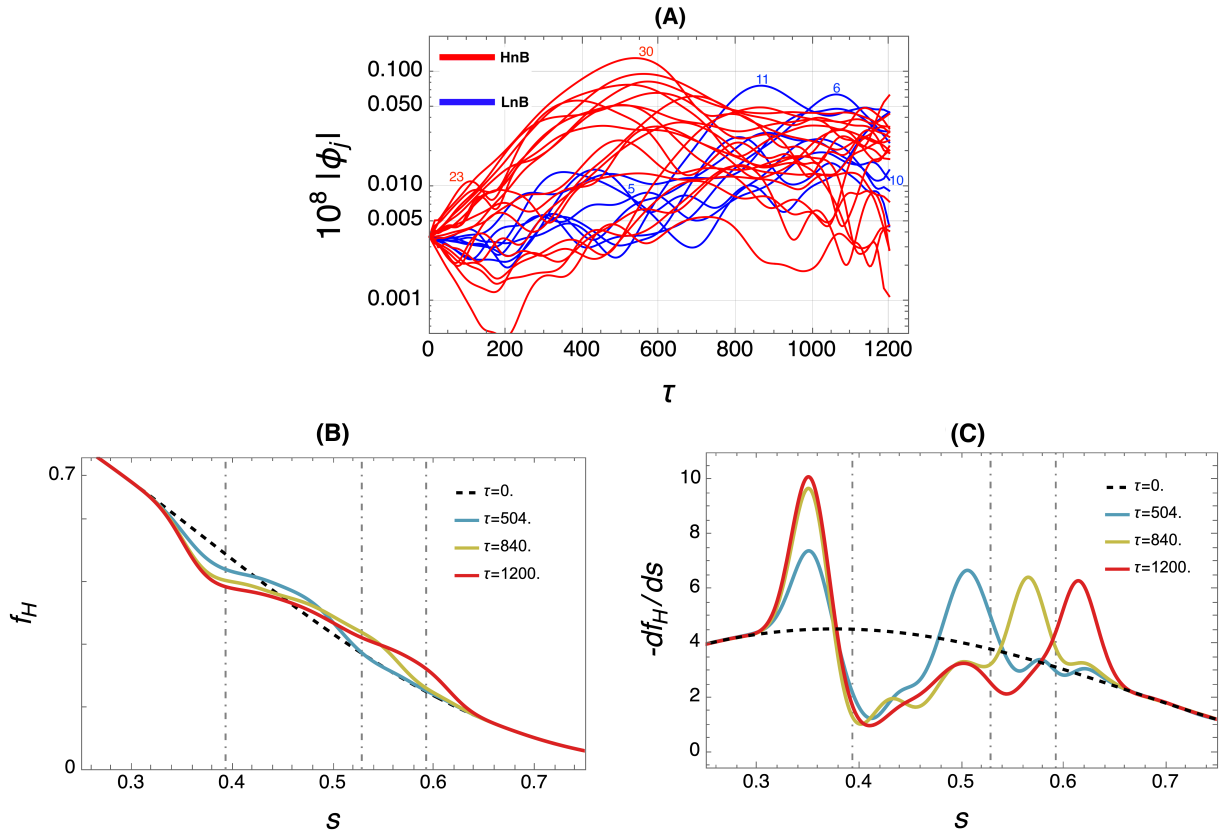


FIG. 2: Panel A — Self-consistent evolution of the 27 modes $|\phi_j(\tau)|$ (examples of mode numbers are also indicated). Panel B — Evolution of EP profile as function of s (different times are indicated in the plot). Gray dashed vertical lines indicate the HnB and LnB resonant regions. Panel C — Evolution of the radial gradient of the EP profile.

(from 3D to 1D), γ_{Dj} result smaller than the normalized linear AE drives Γ_{Dj} , and their ratio roughly corresponds to the fraction of the most resonant particles for each resonance [1, 54]. We stress how the effective growth rates are $\gamma_j = \gamma_{Dj} - \gamma_{dj}$, where the damping are defined by scaling the AE damping Γ_{dj} (provided by the background plasma and not by the resonant EP [55]), i.e. $\gamma_{dj} \equiv \Gamma_{dj}\omega_j/\Omega_j$, where Ω_j denotes the correspondent AE frequency.

Indicating by (x_i, s_i) a single particle position in the phase space, the reduced nonlinear self-consistent equations for EP relaxation (N and M indicates the total number of particles and modes, respectively) reads

$$\dot{x}_i = (1 - s_i)/\ell^* , \quad (3a)$$

$$\dot{s}_i = -\ell^* \sum_{j=1}^M (i \ell_j \phi_j e^{i\ell_j x_i} + c.c.) , \quad (3b)$$

$$\dot{\phi}_j = -i\phi_j - \gamma_{dj}\phi_j + \frac{i\eta}{2\ell_j^2 N} \sum_{i=1}^N e^{-i\ell_j x_i} , \quad (3c)$$

which correspond to the Hamiltonian formulation of the BoT model [29, 41] (the dot denotes differentiation with respect to the normalized time τ).

The ITER 15MA baseline scenario is taken as reference case [28] (see also [55–57]). The initial EP profile is described by Eq.(1) with $B_1 \simeq 0.5$, $B_2 \simeq -1.2$ and $B_3 \simeq 3.2$, and the least damped 27 toroidal AEs, described in the linear analysis of [55], are included in the dynamics. Specifically, $n_{AE} \in [12, 30]$ for the main (high- n_{AE}) branch (HnB) and $n_{AE} \in [5, 12]$ for the low branch (LnB). In FIG.1—A, we plot $f_H^0(s)$ from Eq.(1) indicating with colored vertical lines the mode resonance positions. The determination of the free parameter η is outlined in some detail in [1, 54] and it results related to the fraction of the most resonant particles. Consistently, we assume $\eta = 0.007$ (with $\ell^* = 400$) throughout this paper. In FIG.1—B, we show the obtained linear drives from Eq.(2) using this value for η and the above mentioned $f_H^0(s)$. We also plot the damping γ_{dj} obtained by scaling data from [28] (as previously described), and the corresponding effective growth rates γ_j . It clearly emerges how part of the HnB and all the LnB results linearly stable (sub-dominant).

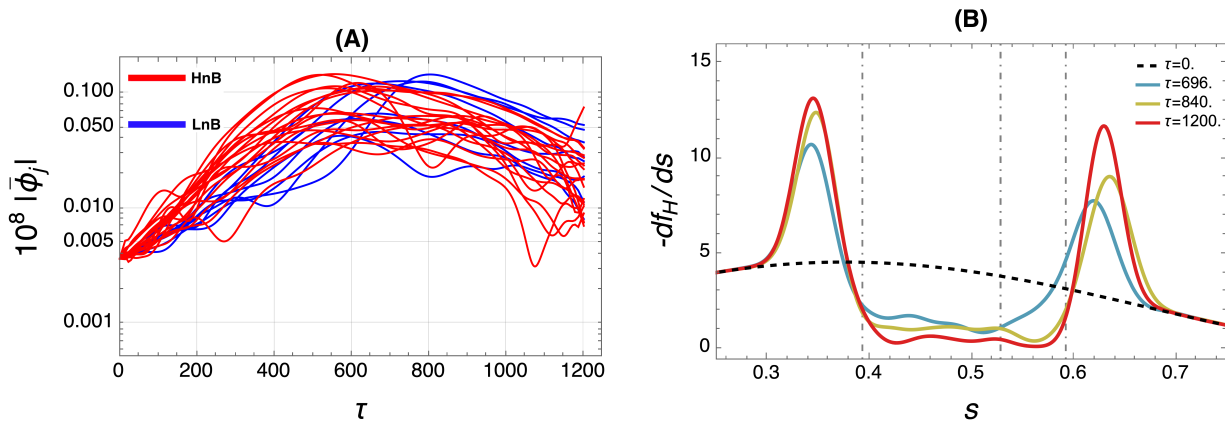


FIG. 3: Benchmark case. Panel A — Plot of the mode self-consistent evolution. Panel B — Plots of the radial gradient of the EP profile. Gray dashed vertical lines indicate the HnB and LnB resonant regions.

Using this setup, Eqs.(3) are evolved in time¹ and the resulting mode profiles are plotted in FIG.2—A. Notably, the stable part of the spectrum is now destabilized resulting excited by an avalanche mechanism (in agreement with [28]). This domino-like excitation is evident when observing the evolution of the distribution function (FIG.2—B) and its derivative with respect to s (FIG.2—C). In particular, a first peak emerges around $s \simeq 0.35$ (related to the excitation of part of HnB), while a second peak (starting in the region of the sub-dominant LnB) is shifting in time toward large s values. This feature characterizes the avalanche-like transport toward the plasma edge, and underlines the relevance of the sub-dominant part of the spectrum due to the domino mode excitation, and, in this work, we provide a detailed description of such a mechanism.

A. Benchmark case

We conclude this section by introducing a second case, derived from the ITER 15MA baseline scenario, in which the stable part of the spectrum is artificially removed. This allows a comparison with the realistic ITER scenario. All the modes are now linearly unstable and simultaneously excited resulting in the evolution outlined in FIG.3—A, where the domino effect is negligible. We stress how the mode saturation levels, by virtue of the growth rate profile, are almost identical to the previous scenario. The evolution of the distribution function gradient is shown in FIG.3—B. The shifting peak which was related to the avalanche dynamics in the ITER scenario is consistently localized around $s = 0.64$ and EP profiles at different times result qualitatively comparable with the well know flattening obtained using QL theory.

III. PHASE-SPACE TRANSPORT

Due to the predominantly resonant nature of transport, the structures characterizing particle dynamics in phase space, such as invariant manifolds, play a crucial role and several techniques can be used for their description. However, this task is inherently complex, as the fluctuation amplitudes have a non-trivial time dependence that must be calculated self-consistently with the evolution of the distribution function. Therefore, great care must be used when applying standard techniques typically used for analyzing periodic dynamical systems, such as surface of section analysis, that require a generalization. The concept of LCS [44] has been introduced to characterize transport processes in complex fluid flows with similar features. LCS generalize structures observed in autonomous and periodic systems, e.g. stable and unstable manifolds, to temporally non-periodic flows. Analogously to these structures, LCS divide the phase space into macro-regions inside where fast mixing phenomena take place. These regions act as barriers to transport over the finite time period that defines the LCS.

¹ In the non-linear simulations of this work, we use a Runge-Kutta (fourth order) algorithm and we set $N = 10^6$, while $x_i(\tau = 0)$ are given uniformly between 0 and 2π and modes are initialized at $\mathcal{O}(10^{-14})$, in order the initial linear regime is guaranteed.

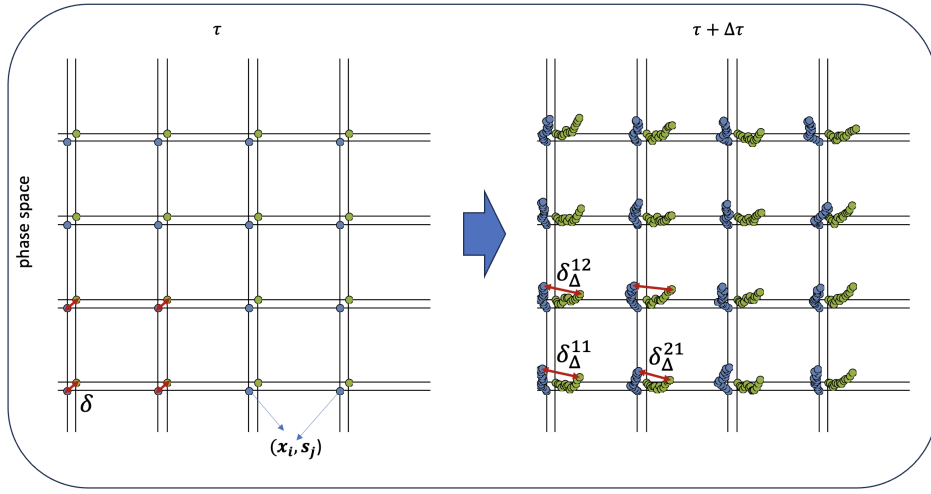


FIG. 4: Cartoon representing the Finite Time Lyapunov Exponent calculation consistently with Eq.(4).

Following [41, 58], we will use the LCS technique to characterize the dynamics in the phase space illuminating the relaxation process described in the previous section. Specifically, we will focus on hyperbolic LCS that organize the flow by either attracting or repelling volume elements over a finite time span, generalizing the concept of stable and unstable manifolds. Various methodologies have been proposed to compute hyperbolic LCS, see e.g. [59] or [60]. Since the largest Finite-Time Lyapunov Exponent (FTLE) at a specific phase space location quantifies the exponential separation between two neighboring initial conditions after a certain time interval $\Delta\tau$, hyperbolic LCS can be determined from the FTLE contour plots, see e.g. [45].

In the following, we employ a test particle approach. Tracer trajectories are evaluated using the assigned potential fields described in the previous sections, i.e. tracers are evolved by means of Eqs.(3a) and (3b) alone. We track markers initialized on two phase-space grids at a given time τ , as depicted in FIG.4. Points of the first grid are denoted as (x_i, s_j) while points on the second grid as (x'_i, s'_j) . The second grid is obtained from the first one through a small translation δ . As the tracers evolve, by the time $\tau + \Delta\tau$, the distance between a point and its corresponding point on the second grid can be denoted as δ_{Δ}^{ij} . The FTLE field $\sigma_{i,j}(\tau, \Delta\tau)$ is readily computed on the first grid as

$$\sigma_{i,j}(\tau, \Delta\tau) = \ln(\delta_{\Delta}^{ij}/\delta)/\Delta\tau. \quad (4)$$

As previously mentioned, hyperbolic LCS are closely linked to the contours of $\sigma_{i,j}$ in the phase-space, especially with 1D peaked structures known as ridges [60]. It is well known that, in a scenario involving a single mode with a constant amplitude, similarly to a pendulum, attractive and repulsive structures will merge into the separatrix. The hyperbolic LCS will reflect this, as shown in [41, 58]. Considering a general non-autonomous dynamical system, multiple intersections occur allowing transport by means of the so called lobe-dynamics, see e.g. [46].

We compute FTLE contours for both the ITER scenario and the benchmark case. We also remark how for $\Delta\tau > 0$ (< 0), the FTLE peaks indicate repulsive (attractive) transport barriers. We plot the contours of the FTLE using $\Delta\tau = \pm 200$ and mode amplitudes at different times. The choice of $\Delta\tau$ requires care (as detailed in [58]) in view of the time scales of the mode evolution. Larger $\Delta\tau$ values generate contour plots with long structures approximating the well-known tangles between stable and unstable manifolds. Smaller values result in simpler structures describing the coherence of the mixing of passive tracers over a shorter time interval [46]. We illustrate how these structures organize the dynamics in the phase-space by analyzing the evolution of markers initialized at $n_{AE} = 5, 18, 26$ resonances.

The analysis of ITER scenario is summarized in FIG.5 and FIG.6. At $\tau = 310$, passive tracers rotate within single resonance structures, as expected [58, 61]. As they rotate, energy is transferred to the modes increasing their amplitude. This process drives an elongation of attractive and repulsive structures that cover ~ 10 resonances at $\tau = 360$. Particles move almost coherently along these structures and resonate with all these modes, efficiently driving them. By $\tau = 430$ attractive and repulsive structures intertwine into a single tangle with $0.35 \lesssim s \lesssim 0.50$. Based on these observations, we can infer that transport within this region (which corresponds to the HnB resonant portion) should exhibit diffusive behavior from that time onward. This will be confirmed by the statistical analysis of the next section. Consequently, the distribution function will slowly form a plateau.

Up to $\tau = 430$, the FTLE contour plots do not exhibit strong ridges in the region $0.50 < s < 0.55$, which is characterized by stable modes while lower ridges are found for $0.57 < s < 0.60$. Consequently, we do not observe any significant transport process in these regions. However, mixing phenomena within the plateau region increase the

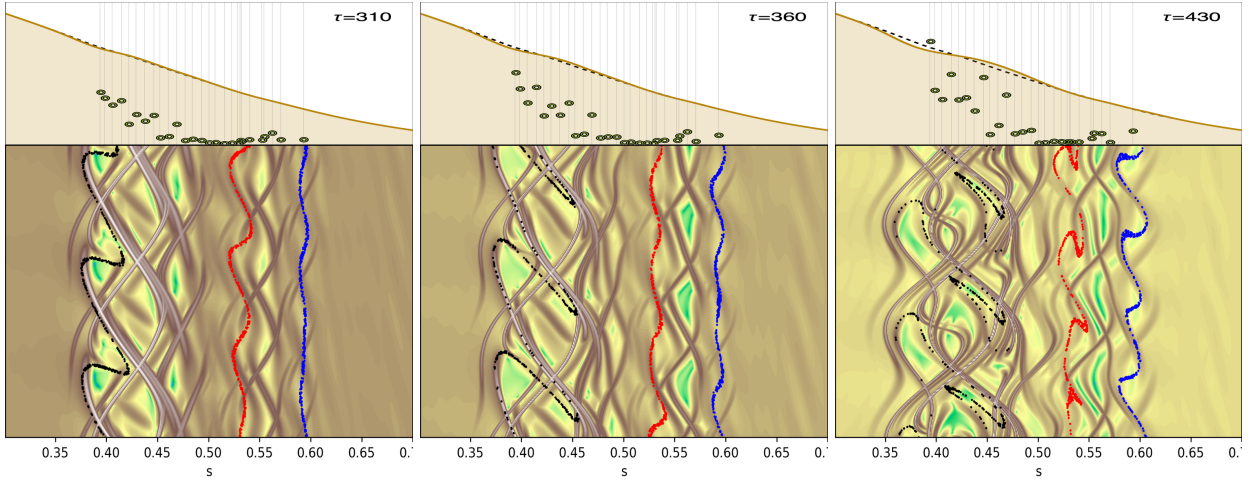


FIG. 5: ITER scenario. Contour plots of the FTLE in the initial phase of the dynamics are plotted in the lower panels with the following Color-scale: $\text{a.u.} +1$. The evolution of the distribution function overlapped on the mode amplitudes (green annulus) in arbitrary units is represented in the upper panels. Three marker populations initialized around the $n_{AE} = 5$ (black), 18 (red) and 26 (blue) are overlapped.

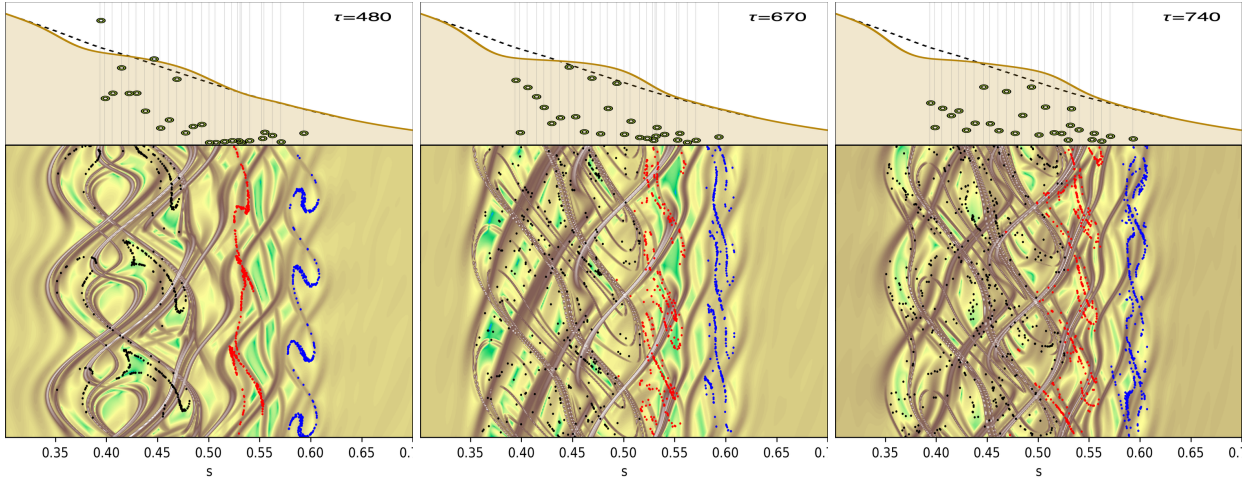


FIG. 6: ITER scenario. Same as FIG.5, but for the late phase of the dynamics.

absolute value of the distribution function gradient and the amplitude of the modes with $s \sim 0.50$ increases, along with the elongated ridges of the FTLE field. This avalanche phenomenon is qualitatively similar to results presented in [18], where they introduce a modification of the QL model in order to take into account the domino-like transport. By $\tau = 480$, FTLE ridges cover a significant portion of the phase-space characterized by stable modes. Consistently, these modes are driven, and the plateau extend to the right while the HnB transfer energy to the LnB (linear stable part of the spectrum) that begins to grow. Moreover, tracers resonating with the HnB (black and red) cover a large region, thus interacting simultaneously with multiple resonances. The trend continues at $\tau = 670$ and $\tau = 740$, leading to an expansion of the region where fast mixing phenomena take place. The resulting nature of the transport will be analyzed in the next section. Once all the modes have sufficiently large amplitude, the phase space is characterized by a unique plateau.

The same methodology can be applied to the benchmark case, and the results are shown in FIG.7. The dynamics until $\tau \sim 550$ includes linear mode saturation and it shows how the tracers follow attractive barriers during their evolution. LCSs overlap already at $\tau = 550$. Consequently, fast mixing phenomena take place and the distribution function exhibits a unique plateau. Modes are almost simultaneously excited and particles interact with the whole spectrum (auto-correlation time) during a time-scale comparable to the single mode trapping time.

Concluding, this study highlighted discrepancies from purely diffusive transport for the analyzed ITER scenario, and further diagnostics will be introduced in the following section in order to characterize such transport peculiarities.

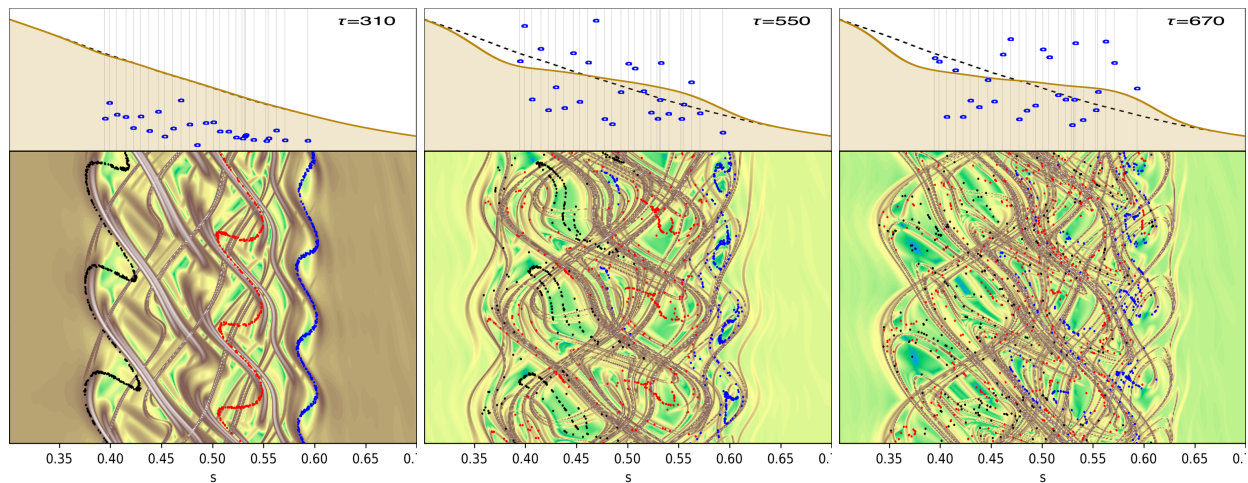


FIG. 7: Benchmark case. Same as FIG.5.

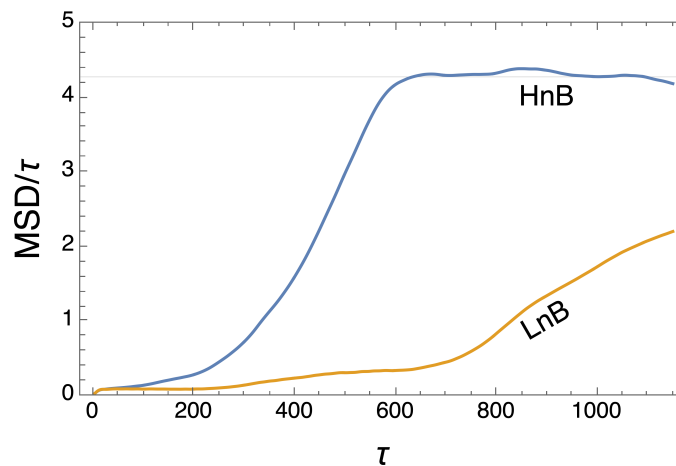


FIG. 8: Plot of MSD/τ (arbitrary units) as a function of τ for tracers initialized in the resonant region of the HnB (blue) and the the LnB (yellow).

IV. DEFINITION OF TRANSPORT REGIMES

When addressing the ITER 15MA baseline scenario, the proposed reduced model introduced in the previous sections effectively highlights the failure of the QL model in characterizing the relaxation process [1]. In this respect, we stress again the importance of the sub-dominant part of the spectrum as the key ingredient yielding deviation from QL predictions. Anyway, we remark that, the decay of the QL assumptions actually does not guarantee the non-applicability of the model, also when strong mode-mode coupling is present (see the review [62] and [12, 63, 64]). The observed discrepancy for the ITER case under investigation, thus, requires a careful analysis of the stochasticization processes underlying the distribution function evolution.

The relaxation process can again be analyzed with test particle analysis. Specifically, we track the mean square displacement as a function of time: $\text{MSD} = \langle [s(\tau) - \langle s(\tau) \rangle]^2 \rangle$, where averages $\langle \dots \rangle$ are taken over the population of test-particles. For completeness, we specify that the following analysis accounts for 10^6 tracers for each run. Different behaviors of the MSD discriminate distinct transport features. In particular, diffusion is characterized by constant MSD/τ (for a different but complementary statistical approach, see [65–68]).

We track the MSD for two distinct tracer populations, namely: test particles initialized in the resonant region of the HnB (from $s_{30} \simeq 0.39$ to $s_{12} \simeq 0.53$), and of the LnB (from s_{12} to $s_5 \simeq 0.59$). In FIG.8, we show the evolution of MSD/τ for such particles consistently with the results of the previous section. It emerges how the first population is characterized by diffusive transport during the post saturation dynamics, where MSD/τ reaches a constant value. Conversely, for the second population, for $\tau > 800$ most of the sub-dominant part of the spectrum is saturated while

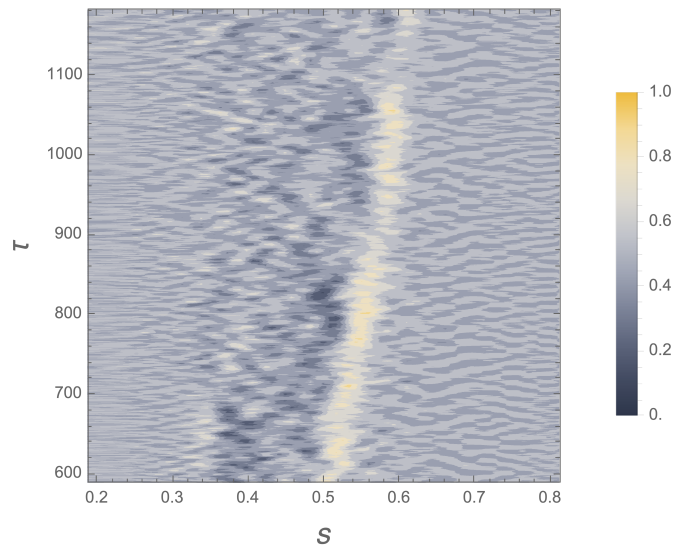


FIG. 9: Contours of the flux divergence (i.e. $\partial_\tau f_H(s)$) for the ITER scenario.

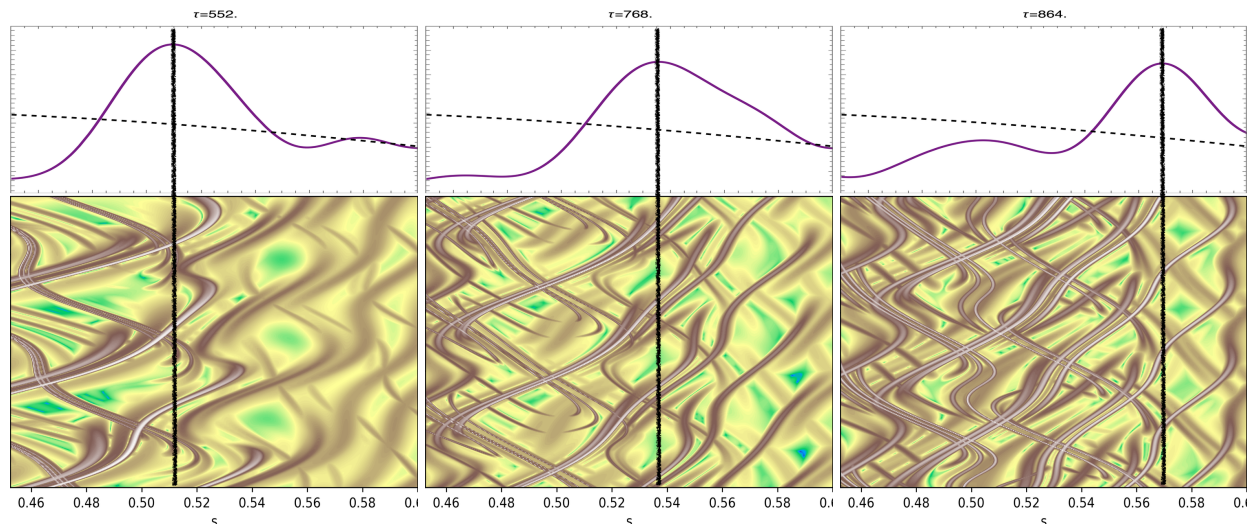


FIG. 10: ITER scenario. Contour plots of the FTLE as in FIG.5 are plotted in the lower panels. The evolution of the derivative of the distribution function is reported in the upper panels (the black dashed line represents the initial time $\tau = 0$). The vertical line highlights the maximum gradient position.

MSD/τ continues to growth. This indicates a non-diffusive, and in this case super-diffusive, transport regime. We underline how in [18] the avalanche phenomena are successfully described using a pure diffusive scheme (line broadened QL model) while this analysis indicates that the domino excitation of the sub-dominant part of the spectrum is linked to a more complex transport phenomenology.

In order to provide further evidence of non diffusive features, let us now analyze the particle fluxes for the ITER scenario. The flux divergence, i.e., $\partial_\tau f_H(s)$, is evaluated by finite differences and is represented in FIG.9. A peaked structure with ballistic-like motion is outlined, consistently with the non-diffusive transport nature described above. The shifting velocity is almost constant and clearly marks a particle flux toward the edge region. In this respect, in FIG.10, we plot the FTLE contours together with the gradient of the distribution function. The highest peaks of the FTLE fields follow the shifting of the distribution function gradient, which results in the domino excitation of the sub-dominant part of the spectrum.

We conclude by stressing how this complete analysis confirms and deepens the results of [28] (and [1]), underlining the non applicability of the QL theory, when addressing the sub-dominant part of the spectrum generating outer EP

redistribution.

V. CONCLUDING REMARKS

In this work, we have provided a detailed examination of the transport mechanisms associated with an avalanche process emerging in the ITER 15MA baseline scenario. Implementing the LCS technique provided a clear visualization of the transport barriers within the phase space of the system. The emergence of transport channels, driven by the formation of a steep gradient in the right tail of the plateau region, underscores the role of non-linear particle-mode interactions. This mechanism strongly differs from the diffusive benchmark introduced, where transport is driven by a globally unstable spectrum leading to strong mode overlaps. The relaxation process has been analyzed by means of the MSD showing how particles exhibit super-diffusive transport. Thus, if stable modes are included in the model, a fully-nonlinear treatment of EP relaxation is required. The ballistic nature of particle transport is also highlighted by the analysis of the fluxes where a peaked structure moving with approximately constant velocity characterizes the dynamics. Concluding, the presented analyses identified specific factors associated with avalanche phenomena, crucial for predicting the onset of non-diffusive transport. These indicators enhance the ability to forecast distinct transport regimes without using non-linear gyrokinetic simulations.

Acknowledgment

The authors would like to acknowledge insightful discussions with Prof. F. Zonca. This work was carried out within the framework of the EUROfusion Consortium and received funding from Euratom research and training programme 2019–2020 under Grant Agreement No. 633053 (Project No. WP19-ER/ENEA-05). This work has been carried out within the framework of the EUROfusion Consortium, funded by the European Union via the Euratom Research and Training Programme (Grant Agreement No 101052200 – EUROfusion; Projects No. ENR-MOD.01.MPG and AC-TSVV.10.MPG). Views and opinions expressed are however those of the author(s) only and do not necessarily reflect those of the European Union or the European Commission. Neither the European Union nor the European Commission can be held responsible for them. This work was supported in part by the Italian Ministry of Foreign Affairs and International Cooperation, grant number CN23GR02 and by the MMNLP project CSN4 of INFN, Italy.

-
- [1] N. Carlevaro, G. Meng, G. Montani, F. Zonca, T. Hayward-Schneider, Ph. Lauber, Z. Lu and X. Wang, *Plasma Phys. Contr. Fus.* **64**, 035010 (2022).
 - [2] W. W. Heidbrink and R. B. White, *Phys. Plasmas* **27**, 030901 (2020).
 - [3] L. Chen and F. Zonca, *Rev. Mod. Phys.* **88**, 015008 (2016).
 - [4] F. Zonca, L. Chen, S. Briguglio, G. Fogaccia, G. Vlad and X. Wang, *New J. Phys.* **17**, 013052 (2015).
 - [5] R. J. Dumont, D. Zarzoso, Y. Sarazin, X. Garbet, A. Strugarek, J. Abiteboul, T. Cartier-Michaud, G. Dif-Pradalier, P. Ghendrih, J.-B. Girardo, V. Grandgirard, G. Latu, C. Passeron and O. Thomine, *Plasma Phys. Contr. Fusion* **55**, 124012 (2013).
 - [6] E. M. Bass and R. E. Waltz, *Phys. Plasmas* **17**, 112319 (2010).
 - [7] F. Zonca, L. Chen, S. Briguglio, G. Fogaccia, A. V. Milovanov, Z. Qiu, G. Vlad and X. Wang, *Plasma Phys. Contr. Fusion* **57**, 014024 (2015).
 - [8] A. Bierwage, K. Shinohara, Y. Todo, N. Aiba, M. Ishikawa, G. Matsunaga, M. Takechi and M. Yagi, *Nature Comm.* **9**, 3282 (2018).
 - [9] P. Lauber, *Phys. Rept.* **533**, 33 (2013).
 - [10] M. Podestà, M. Gorelenkova and R. B. White, *Plasma Phys. Contr. Fusion* **56**, 055003 (2014).
 - [11] R. E. Waltz, E. M. Bass, W. W. Heidbrink and M. A. VanZeeland, *Nucl. Fusion* **55**, 123012 (2015).
 - [12] N. N. Gorelenkov, V. N. Duarte, M. Podesta and H. L. Berk, *Nucl. Fus.* **58**, 082016 (2018).
 - [13] N. N. Gorelenkov, W. W. Heidbrink, G. J. Kramer, J. B. Lestz, M. Podesta, M. A. Van Zeeland and R. B. White, *Nuclear Fusion* **56**, 112015 (2016).
 - [14] Ph. Lauber, M. Falessi, G. Meng, T. Hayward-Schneider, V. A. Popa, F. Zonca and M. Schneider, *Nucl. Fus.* **64**, 096010 (2024).
 - [15] G. Meng, Ph. Lauber, Z. Lu, A. Bergmann and M. Schneider, *Nucl. Fus.* (in press) (2024).
 - [16] M.V. Falessi, L. Chen, Z Qiu and F Zonca, *New J. Physics* **25**, 123035 (2023).
 - [17] M.A. Van Zeeland, C.S. Collins, W.W. Heidbrink, M.E. Austin, X.D. Du, V.N. Duarte, A. Hyatt, G. Kramer, N. Gorelenkov, B. Grierson, D. Lin, A. Marinoni, G. McKee, C. Muscatello, C. Petty, C. Sung, K. E. Thome, M. Walker and Y.B. Zhu, *Nucl. Fus.* **59**, 086028 (2019).

- [18] H. L. Berk, B. N. Breizman, J. Fitzpatrick and H. V. Wong, *Nucl. Fusion* **35**, 1661 (1995).
- [19] H. L. Berk, B. N. Breizman, J. Fitzpatrick, M. S. Pekker, H. V. Wong and K. L. Wong, *Phys. Plasmas* **3**, 1827 (1996).
- [20] K. Ghantous, N. N. Gorelenkov, H. L. Berk, W. W. Heidbrink and M. A. Van Zeeland, *Phys. Plasmas* **19**, 092511 (2012).
- [21] K. Ghantous, H. L. Berk and N. N. Gorelenkov, *Phys. Plasmas* **21**, 032119 (2014).
- [22] C. Bourdelle, X. Garbet, F. Imbeaux, A. Casati, N. Dubuit, R. Guirlet and T. Parisot, *Phys. Plasmas* **14**, 112501 (2007).
- [23] C. Bourdelle, J. Citrin, B. Baiocchi, A. Casati, P. Cottier, X. Garbet, F. Imbeaux and JET Contributors, *Plasma Phys. Contr. Fusion* **58**, 014036 (2016).
- [24] M. Podestà, M. Gorelenkova, E. D. Fredrickson, N. N. Gorelenkov and R. B. White, *Phys. Plasmas* **23**, 056106 (2016).
- [25] M. V. Falessi and F. Zonca, *Phys. Plasmas* **26**, 022305 (2019).
- [26] N. Carlevaro, F. Finelli and G. Montani, *Europhys. Lett.* **127**, 25002 (2019).
- [27] V.N. Duarte, H.L. Berk, N.N. Gorelenkov, W.W. Heidbrink, G.J. Kramer, R. Nazikian, D.C. Pace, M. Podestà, B.J. Tobias and M.A. Van Zeeland, *Nucl. Fus.* **57**, 054001 (2017).
- [28] M. Schneller, Ph. Lauber and S. Briguglio, *Plasma Phys. Contr. Fusion* **58**, 014019 (2016).
- [29] N. Carlevaro, A. V. Milovanov, M. V. Falessi, G. Montani, D. Terzani and F. Zonca, *Entropy* **18**, 143 (2016).
- [30] G. Meng, N.N. Gorelenkov, V.N. Duarte, H.L. Berk, R.B. White, A. Bhattacharjee and X.G. Wang, *Nucl. Fus.* **58**, 082017 (2018).
- [31] G. Zacharegkas, H. Isliker and L. Vlahos, *Phys. Plasmas* **23**, 112119 (2016).
- [32] H. L. Berk and B. N. Breizman, *Phys. Fluids B* **2**, 2226 (1990).
- [33] H. L. Berk and B. N. Breizman, *Phys. Fluids B* **2**, 2235 (1990).
- [34] H. L. Berk and B. N. Breizman, *Phys. Fluids B* **2**, 2246 (1990).
- [35] L. Chen and F. Zonca, *Phys. Plasmas* **20**, 055402 (2013).
- [36] C. Krafft and A. S. Volokitin, *Plasma Phys. Contr. Fus.* **62**, 024007 (2020).
- [37] Sh. Abbasi Rostami, S. M. Khorashadizadeh and A. R. Niknam, *Plasma Phys. Contr. Fus.* **62**, 115004 (2020).
- [38] C. Krafft and A. Volokitin, *Eur. Phys. J. D* **68**, 370 (2014).
- [39] R. B. White, V. N. Duarte, N. N. Gorelenkov, E. D. Fredrickson and M. Podesta, *Phys. Plasmas* **27**, 022117 (2020).
- [40] V. N. Duarte, N. N. Gorelenkov, R. B. White and H. L. Berk, *Phys. Plasmas* **26**, 120701 (2019).
- [41] N. Carlevaro, M. V. Falessi, G. Montani and F. Zonca, *J. Plasma Phys.* **81**, 495810515 (2015).
- [42] Ph. Lauber, S. Günter, A. Könies and S.D. Pinches, *J. Comp. Phys.* **226**, 447 (2007).
- [43] S.D. Pinches, L.C. Appel, J. Candy, S.E. Sharapov, H.L. Berk, D. Borba, B.N. Breizman, T.C. Hender, K.I. Hopcraft, G.T.A. Huysmans and others, *Computer Phys. Comm.* **111**, 133 (1998).
- [44] G. Haller, *Annual Review of Fluid Mechanics* **47**, 137–162 (2015).
- [45] M. V. Falessi, F. Pegoraro and T. J. Schep, *J. Plasma Phys.* **81**, 495810505 (2015).
- [46] G. Di Giannatale, M.V. Falessi, D. Grasso, F. Pegoraro and T.J. Schep, *Phys. Plasmas* **25**, 052306 (2018).
- [47] G. Di Giannatale, M. V. Falessi, D. Grasso, F. Pegoraro and T. J. Schep, *Phys. Plasmas* **25**, 052307 (2018).
- [48] F. Pegoraro, D. Bonfiglio, S. Cappello, G. Di Giannatale, M. V. Falessi, D. Grasso and M. Veranda, *Plasma Phys. Contr. Fusion* **61**, 044003 (2019).
- [49] K. Padberg, T. Hauff, F. Jenko and O. Junge, *New J. Physics* **9**, 400 (2007).
- [50] E. L. Rempel, A. C. L. Chian, S. de SA Silva, V. Fedun, G. Verth, R. A. Miranda and M. Gošić, *Rev. Mod. Plasma Phys.* **7**, 32 (2023).
- [51] D. Borgogno, D. Grasso, F. Pegoraro and T. J. Schep, *Phys. Plasmas* **18**, 102307 (2011).
- [52] G. Di Giannatale, D. Bonfiglio, S. Cappello, L. Chacón and M. Veranda, *Nucl. Fus.* **61**, 076013 (2021).
- [53] X. Wang, S. Briguglio, A. Bottino, M. Falessi, T. Hayward-Schneider, Ph Lauber, A. Mishchenko, L. Villard and F. Zonca, *Plasma Phys. Contr. Fus.* **65**, 074001 (2023).
- [54] N. Carlevaro, G. Montani, M.V. Falessi and P. Lauber, in *48th EPS Conference on Plasma Physics* **46A**, P5a.113 (2022).
- [55] Ph. Lauber, *Plasma Phys. Contr. Fusion* **57**, 054011 (2015).
- [56] M. Schneller, P. Lauber, M. Brüdgam, S.D. Pinches and S. Günter, *Nucl. Fusion* **52**, 103019 (2012).
- [57] M. Schneller, P. Lauber, R. Bilato, M. García-Muñoz, M. Brüdgam, S. Günter and the ASDEX Upgrade Team, *Nucl. Fusion* **53**, 123003 (2013).
- [58] N. Carlevaro, , G. Montani and M.V. Falessi, *J. Plasma Phys.* **86**, 845860401 (2020).
- [59] G. Haller, *Physica D* **240**, 574 (2011).
- [60] S. C. Shadden, F. Lekien and J. E. Marsden, *Physica D* **212**, 271 (2005).
- [61] J. L. Tennyson, J. D. Meiss and P. J. Morrison, *Physica D* **71**, 1 (1994).
- [62] D.F. Escande, D. Bënisti, Y. Elskens, D. Zarzoso and D. Doveil, *Rev. Mod. Plasma Phys.* **2**, 9 (2018).
- [63] N. Besse, Y. Elskens, D. F. Escande and P. Bertrand, *Plasma Phys. Contr. Fus.* **53**, 025012 (2011).
- [64] G. Montani, F. Cianfrani and N. Carlevaro, *Plasma Phys. Contr. Fus.* **61**, 078018 (2019).
- [65] A. Volokitin and C. Krafft, *Plasma Phys. Contr. Fusion* **54**, 085002 (2012).
- [66] A. Zagorodny, V. Zasenko, J. Weiland and I. Holod, *Phys. Plasmas* **10**, 58 (2003).
- [67] C. Krafft, A. S. Volokitin and G. Gauthier, *Fluids* **4**, 69 (2019).
- [68] A. S. Volokitin and C. Krafft, *ApJ* **833**, 166 (2016).